

## Identifying chaotic electron trajectories in a helical-wiggler free-electron laser

A. Bourdier\*

*Commissariat à l'Energie Atomique, Centre d'Etudes de Bruyères-le-Châtel,  
Boîte Postale 12, 91680 Bruyères-le-Châtel, France*

L. Michel-Lours

*Laboratoire de Physique des Milieux Ionisés, Ecole Polytechnique, 91128 Palaiseau Cedex, France  
(Received 16 September 1993)*

When taking into account the equilibrium self-fields of the beam, it is confirmed that the motion of an electron in a helical wiggler with guide field may be chaotic. There is evidence of chaos from numerical calculations of nonzero Lyapunov exponents using different approaches of Benettin's method which are described and compared. Very accurate Poincaré maps are also performed.

PACS number(s): 41.60.Cr, 05.45.+b

### I. INTRODUCTION

The electron orbits in a helical wiggler are examined in the presence of a guide field. When the self-fields of the beam are taken into account, some trajectories become chaotic.

The nonintegrability of the electron motion is demonstrated in this work by calculating nonzero Lyapunov exponents. These are derived by using different approaches of Benettin's [1] method which are described in detail. The largest Lyapunov exponent is estimated considering two trajectories with very close initial conditions and also by using the tangent vector method. The good agreement between the different results makes us confident that, in some circumstances, a nonzero Lyapunov exponent exists.

Poincaré maps are also generated very accurately, to confirm that some trajectories are chaotic. The results obtained are similar to those of Chen and Davidson [2]. Local Lyapunov exponents [3] are also calculated. The resulting mixing time for the trajectories shows that the predicted chaos can be a proper problem in an experiment.

### II. THEORETICAL FORMULATION OF THE PROBLEM

Consider the motion of a relativistic electron in a uniform axial field  $B_0\mathbf{e}_z$ , a constant amplitude helical wiggler magnetic field  $\mathbf{B}_\omega = -B_\omega(\mathbf{e}_x \cos k_\omega z + \mathbf{e}_y \sin k_\omega z)$ , and the self-electric and self-magnetic fields produced by a relativistic non-neutral electron beam [2]. The beam is assumed to have an average axial velocity  $V_b\mathbf{e}_z$ , where  $V_b$  is a constant. A uniform density profile for the beam is considered. The self-fields can be expressed as [2,4]

$$\mathbf{E}_s = -\frac{m\omega_{pb}^2}{2e}(x\mathbf{e}_x + y\mathbf{e}_y), \quad (1)$$

$$\mathbf{B}_s = \frac{m\omega_{pb}^2\beta_b}{2ec}(y\mathbf{e}_x - x\mathbf{e}_y), \quad (2)$$

where  $\omega_{pb}^2 = n_b e^2 / m \epsilon_0$ ,  $\beta_b = V_b / c$ , and  $n_b$  is the electron density in the laboratory frame.

The scalar and vector potentials,  $\phi_s$  and  $\mathbf{A}$ , can be defined by

$$\phi_s = m\frac{\omega_{pb}^2}{4e}(x^2 + y^2), \quad (3)$$

$$\mathbf{A} = B_0 x \mathbf{e}_y + A_\omega (\mathbf{e}_x \cos k_\omega z + \mathbf{e}_y \sin k_\omega z) + \frac{\beta_b}{c} \phi_s \mathbf{e}_z, \quad (4)$$

with  $A_\omega = B_\omega / k_\omega$ . Let us examine electron trajectories. The single-electron Hamiltonian is

$$H = [(\mathbf{P} + e\mathbf{A})^2 c^2 + m^2 c^4]^{1/2} - e\phi_s \quad (5)$$

$$= \gamma mc^2 - e\phi_s, \quad (6)$$

where  $\gamma$  is the relativistic Lorentz mass factor and  $\mathbf{P}$  the canonical momentum.

Introducing the following dimensionless variables and parameters,

$$\hat{x}_i = k_\omega x_i, \quad \hat{P}_i = \frac{P_i}{mc}, \quad \tau = ck_\omega t, \quad a_\omega = \frac{eA_\omega}{mc},$$

$$\hat{H} = \frac{H}{mc^2}, \quad \hat{\omega}_{pb} = \frac{\omega_{pb}}{ck_\omega}, \quad \hat{\Phi}_s = \frac{e\Phi_s}{mc^2}, \quad \hat{\Omega}_c = \frac{eB_\omega}{mck_\omega},$$

the Hamilton equations can be written as

\*Also at Laboratoire de Physique des Milieux Ionisés, Ecole Polytechnique, 91128 Palaiseau Cedex, France.

$$\begin{aligned} \frac{d\hat{x}}{d\tau} &= \frac{\partial \hat{H}}{\partial \hat{P}_x} = \frac{1}{\gamma} (\hat{P}_x + a_\omega \cos \hat{z}), \\ \frac{d\hat{y}}{d\tau} &= \frac{\partial \hat{H}}{\partial \hat{P}_y} = \frac{1}{\gamma} (\hat{P}_y + \hat{\Omega}_c \hat{x} + a_\omega \sin \hat{z}), \\ \frac{d\hat{z}}{d\tau} &= \frac{\partial \hat{H}}{\partial \hat{P}_z} = \frac{\hat{P}_z}{\gamma} + \frac{\beta_b}{\gamma} \hat{\Phi}_s, \end{aligned} \tag{7}$$

$$\frac{d\hat{P}_x}{d\tau} = -\frac{\partial \hat{H}}{\partial \hat{x}} = -\hat{\Omega}_c \frac{d\hat{y}}{d\tau} - \hat{x} \beta_b \frac{\hat{\omega}_{pb}^2}{2} \frac{d\hat{z}}{d\tau} + \hat{x} \frac{\hat{\omega}_{pb}^2}{2},$$

$$\frac{d\hat{P}_y}{d\tau} = -\frac{\partial \hat{H}}{\partial \hat{y}} = -\hat{y} \beta_b \frac{\hat{\omega}_{pb}^2}{2} \frac{d\hat{z}}{d\tau} + \hat{y} \frac{\hat{\omega}_{pb}^2}{2},$$

$$\frac{d\hat{P}_z}{d\tau} = -\frac{\partial \hat{H}}{\partial \hat{z}} = a_\omega \left[ \frac{d\hat{x}}{d\tau} \sin \hat{z} - \frac{d\hat{y}}{d\tau} \cos \hat{z} \right].$$

This set of equations is solved numerically using a fourth-order Runge-Kutta method. Figure 1 shows the projection of the electron motion on the  $(\hat{x}, \hat{y})$  plane in the case of some initial conditions (in this case,  $\Omega_c$  is smaller than its critical value). The motion looks “chaotic” for high beam densities and becomes more and more regular as the density decreases. At this stage, one can conclude that the chaos seems to be strongly correlated with the density of the beam.

Figure 2 shows two very close electron trajectories when the density of the beam is assumed to be zero, and, again, when  $\Omega_c$  is smaller than its critical value. Figure 3, in contrast, shows two trajectories starting from the same initial conditions as in Fig. 2, but for a high-density beam case,  $n_b = 2 \times 10^{11} \text{ cm}^{-3}$ , while all other parameters are as those in Fig. 2. A strong divergence between the

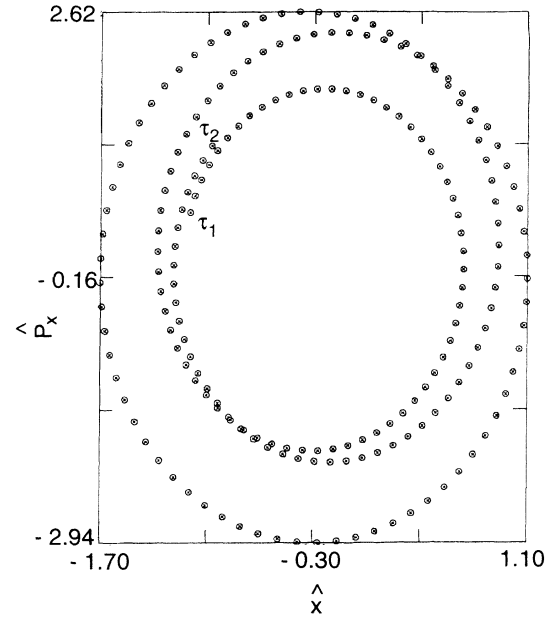


FIG. 2. Projection of two nearby electron trajectories on the  $(\hat{x}, \hat{y})$  plane, for  $\beta_b = 0.91$ ,  $B_0 = 0.715 \text{ T}$ ,  $B_\omega = 715 \text{ G}$ ,  $\hat{\Omega}_c = 2$ ,  $\hat{H} = 3$  between the two times  $\tau_1 = 602$  and  $\tau_2 = 630$ , and for the following initial conditions:  $\hat{x}_1 = \hat{x}_2 = -0.25$ ,  $\hat{y}_1 = \hat{y}_2 = -0.93$ ,  $\hat{z}_1 = \hat{z}_2 = 0$ ,  $\hat{P}_{x_1} = \hat{P}_{x_2} = 1.85$ ,  $\hat{P}_{y_1} = 0.5$ ,  $\hat{P}_{y_2} = \hat{P}_{y_1} (1 + 5 \times 10^{-8})$ ,  $\hat{P}_{z_1} = \hat{P}_{z_2} = 1.97$ .

two trajectories can be observed. The corresponding Lyapunov exponent has been calculated in order to check whether the two trajectories have an exponential rate of divergence. First, the nonzero Lyapunov exponent is calculated using a first approach of Benettin’s method [1,5]. We consider the two trajectories having an initial tangen-

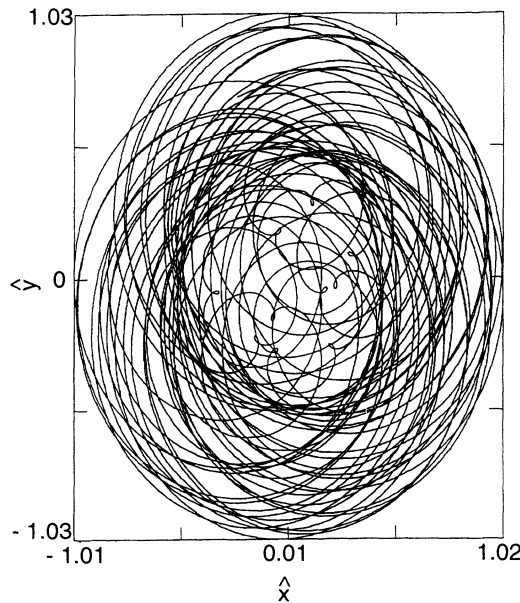


FIG. 1. Projection of an electron trajectory on the  $(\hat{x}, \hat{y})$  plane, for  $n_b = 2 \times 10^{11} \text{ cm}^{-3}$ ,  $\beta_b = 0.91$ ,  $B_0 = 0.715 \text{ T}$ ,  $B_\omega = 715 \text{ G}$ ,  $\hat{\Omega}_c = 2$ ,  $\hat{H} = 3$ , and for the following initial conditions:  $\hat{x} = -0.25$ ,  $\hat{y} = -0.93$ ,  $\hat{z} = 0$ ,  $\hat{P}_x = 1.85$ ,  $\hat{P}_y = 0.5$ ,  $\hat{P}_z = 1.97$ .

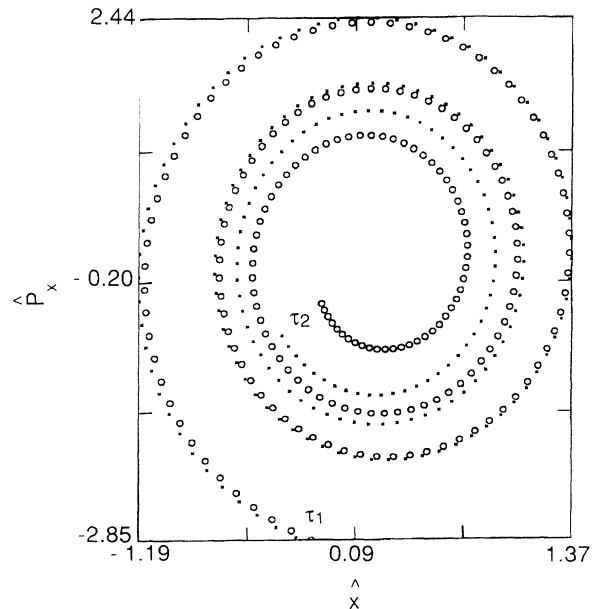


FIG. 3. Projection of two nearby electron trajectories on the  $(\hat{x}, \hat{y})$  plane, for  $n_b = 2 \times 10^{11} \text{ cm}^{-3}$ ,  $\beta_b = 0.91$ ,  $B_0 = 0.715 \text{ T}$ ,  $B_\omega = 715 \text{ G}$ ,  $\hat{\Omega}_c = 2$ ,  $\hat{H} = 3$ , between the two times  $\tau_1 = 602$  and  $\tau_2 = 630$ , and for the same initial conditions as Fig. 2.

tial vector with norm  $d_0$ . A sequence of distances  $d_n$  corresponding to these trajectories is calculated numerically. For every fixed time interval  $\Delta\tau$ , or for every fixed distance ratio  $d_n/d_0 \approx 2$ , we renormalize  $d_n$  to  $d_0$ ; that is to say, we consider another trajectory such that the new initial conditions have an initial tangential vector with norm  $d_0$ .

The Lyapunov exponent is defined as

$$\sigma = \lim_{\substack{n \rightarrow \infty \\ d_0 \rightarrow 0}} \frac{1}{\tau} \sum_n \ln \frac{d_n}{d_0} \tag{8}$$

and its approximate numerical values, as obtained in our calculations for finite  $n$  and  $d_0$ , are shown in Fig. 4. The convergence of our results with respect to  $d_0$  was verified.

The Lyapunov exponent is also calculated using another approach consisting of integrating the differential equation on the tangent vector [1]  $w_i = (x_i - x_j)$ , where the  $x_j$  are the coordinates of a point on a trajectory at time  $\tau$  defined by the initial condition  $\mathbf{x}_0$ , and  $x_i$  are the coordinates of a point on a nearby trajectory at the same time,  $\tau$ , determined by the initial condition  $\mathbf{x}_0 + \Delta\mathbf{x}_0$ . The time evolution for  $\mathbf{w}$  is found by linearizing the equation

$$\frac{d\mathbf{x}_i}{d\tau} = V_i(\mathbf{x}) \tag{9}$$

to obtain

$$\frac{d\mathbf{w}}{d\tau} = \mathbf{M}(\mathbf{x}(\tau)) \cdot \mathbf{w} , \tag{10}$$

where

$$\mathbf{M} = \frac{\partial \mathbf{V}}{\partial \mathbf{x}} . \tag{11}$$

By integrating Eq. (10) numerically, we calculate the quantity  $d = \|\mathbf{w}(\tau)\|$ , leading to  $d_n$  when renormalizations are necessary. Then, the Lyapunov exponent is given by Eq. (8). In most cases, renormalizations are necessary as  $d$  becomes too large. They were performed every fixed

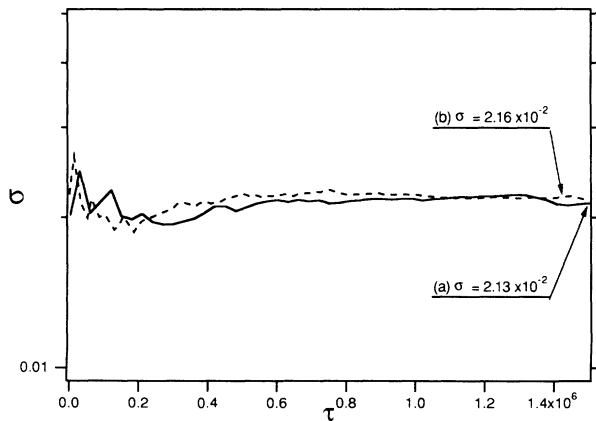


FIG. 4. Lyapunov exponent corresponding to the trajectories shown in Fig. 3, when integrating two trajectories and renormalizing (a) every fixed time  $\Delta\tau=30$  or (b) every fixed distance ratio  $d_n/d_0=2.7$ .

time interval or distance ratio  $d/d_0$ .

The curve I in Fig. 5 shows the numerical results obtained for the Lyapunov coefficient when the high beam density is considered. The curve II, in contrast, shows that, when the self-fields are neglected, the Lyapunov exponent goes to zero as time increases. In this case, the problem is integrable [2,6,7].

With the linearized set of equations, only one limit must be taken ( $d_0$  does not have to be small). Still, the Jacobian matrix  $\mathbf{M}$  can be very complicated in some cases. When two trajectories are considered, the accuracy of the numerical integration of Eq. (9) can be very easily tested using the constants of motion. Nearly the same Lyapunov exponent has been obtained with the different approaches and the different renormalization ways. This makes us confident in the fact that our dynamical system does have a positive Lyapunov exponent.

Another physical situation was considered which is less chaotic for higher currents ( $\Omega_c$  larger than its critical value). A nonzero Lyapunov exponent has been calculated from two trajectories with very close initial conditions [Fig. 6(a)]. It has also been derived by integrating the differential equation on the tangent vector [Fig. 6(b)]. In the next part, we show how a second constant of motion can be found in order to simplify the problem.

The energy of the system is the first constant of motion, as  $H$  does not depend explicitly on time. In order to reduce the dimension of the phase space, a second constant can be easily found using Noether's theorem. It states that if the Lagrangian  $L$  of a system is invariant under the infinitesimal transformation [8]

$$t \rightarrow t + \varepsilon' \vartheta(t, \mathbf{r}), \quad \mathbf{r} \rightarrow \mathbf{r} + \varepsilon' \boldsymbol{\eta}(t, \mathbf{r}) ,$$

where  $\varepsilon'$  is a small dimensionless parameter; then

$$\frac{\partial L}{\partial v} \boldsymbol{\eta} + \left[ L - \mathbf{v} \cdot \frac{\partial L}{\partial \mathbf{v}} \right] \vartheta = \text{const} . \tag{12}$$

For convenience, another gauge,

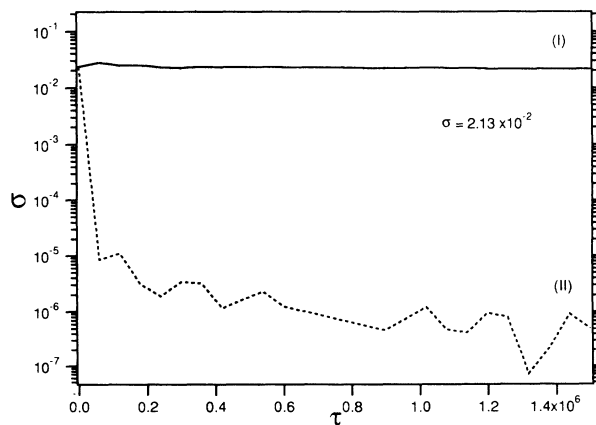


FIG. 5. Lyapunov exponents correspondent to the trajectories shown in Figs. 3 (curve I) and 2 (curve II), when integrating the linearized equations and renormalizing every fixed time  $\Delta\tau=30$ .

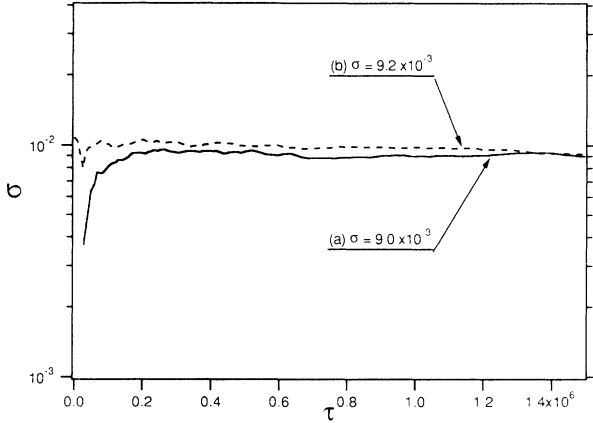


FIG. 6. Lyapunov exponent calculated for  $n_0 = 3.2 \times 10^{12} \text{ cm}^{-3}$ ,  $\beta_0 = 0.93$ ,  $B_0 = 1.42 \text{ T}$ ,  $B_\omega = 710 \text{ G}$ ,  $\Omega_c = 4$ ,  $H = 3$  using two different approaches, the first considering two trajectories with the following initial conditions: (a)  $\hat{x}_1 = \hat{x}_2 = -0.25$ ,  $\hat{y}_1 = \hat{y}_2 = 0.72$ ,  $\hat{z}_1 = \hat{z}_2 = 0$ ,  $\hat{P}_{x_1} = \hat{P}_{x_2} = -2.88$ ,  $\hat{P}_{y_1} = 0.99$ ,  $\hat{P}_{y_2} = \hat{P}_{y_1} (1 + 5 \times 10^{-7})$ ,  $\hat{P}_{z_1} = \hat{P}_{z_2} = 1.45$  (b) the second considering the first trajectory and integrating the linearized equations. Renormalizations are performed every fixed distance ratio  $d_n/d_0 = 2.7$ .

$$\tilde{\mathbf{A}} = \left[ -B_0 \frac{y}{2} + A_\omega \cos k_\omega z \right] \mathbf{e}_x + \left[ B_0 \frac{x}{2} + A_\omega \sin k_\omega z \right] \mathbf{e}_y + \frac{\beta_0}{c} \phi_s \mathbf{e}_z, \quad (13)$$

and the following screw transformation,  $t \rightarrow t$ ,  $x \rightarrow x + \varepsilon' k_\omega y$ ,  $y \rightarrow y - \varepsilon' k_\omega x$ ,  $z \rightarrow z - \varepsilon'$ , were used. The Lagrangian of the system is invariant under the transformation when neglecting terms of  $O(\varepsilon'^2)$ . Since  $\vartheta = 0$  and  $\eta = (k_\omega y, -k_\omega x, -1)$ , a second constant of motion is

$$K = \tilde{P}_x k_\omega y - \tilde{P}_y k_\omega x - \tilde{P}_z, \quad (14)$$

where the  $\tilde{P}_i$ 's are the components of the canonical momentum in the new gauge. To transform the constant of motion in terms of the first gauge, the following invariance relation is used:

$$\mathbf{p} = \mathbf{P} + e \mathbf{A} = \tilde{\mathbf{P}} + e \tilde{\mathbf{A}}. \quad (15)$$

The constant of motion becomes

$$K = k_\omega (y P_x - x P_y) + \frac{1}{2} e B_0 k_\omega (y^2 - x^2) - P_z. \quad (16)$$

This constant of motion can also be found by performing three canonical transformations. They show that when the self-fields are neglected, the system is integrable [2,6,7]. One of these transformations consists in choosing  $-K$  as a new momentum ( $P_{z'}$ ). The product of these three transformations is the transformation given by Chen and Davidson [2], namely,

$$x = \left[ \frac{2P_\varphi}{m\Omega_c} \right]^{1/2} \sin(\varphi + k_\omega z') - \left[ \frac{2P_\Psi}{m\Omega_c} \right]^{1/2} \cos(\Psi - k_\omega z'), \quad (17)$$

$$y = \left[ \frac{2P_\Psi}{m\Omega_c} \right]^{1/2} \sin(\Psi - k_\omega z') - \left[ \frac{2P_\varphi}{m\Omega_c} \right]^{1/2} \cos(\varphi + k_\omega z'), \quad (18)$$

$$z = z', \quad (19)$$

$$P_x = (2m\Omega_c P_\varphi)^{1/2} \cos(\varphi + k_\omega z'), \quad (20)$$

$$P_y = (2m\Omega_c P_\Psi)^{1/2} \cos(\Psi - k_\omega z'), \quad (21)$$

$$P_z = P_{z'} - k_\omega P_\varphi + k_\omega P_\Psi. \quad (22)$$

with  $\Omega_c = eB_\omega/m$ . The following dimensionless parameters and variables are introduced:

$$\hat{\Omega}_c = \frac{\Omega_c}{ck_\omega}, \quad a_\omega = \frac{eA_\omega}{mc}, \quad \hat{\phi}_s = \frac{e\phi_s}{mc^2}, \quad \hat{H} = \frac{H}{mc^2},$$

$$\hat{P}_{z'} = \frac{P_{z'}}{mc}, \quad \hat{P}_\varphi = \frac{k_\omega P_\varphi}{mc}, \quad \hat{P}_\Psi = \frac{k_\omega P_\Psi}{mc},$$

$$\hat{z}' = k_\omega z', \quad \tau = ck_\omega t.$$

The Hamiltonian in the new variables becomes

$$\hat{H}(\varphi, \Psi, \hat{P}_\varphi, \hat{P}_\Psi, \hat{P}_{z'}) = -\hat{\phi}_s + \{ 2\hat{\Omega}_c \hat{P}_\varphi + a_\omega^2 + 2a_\omega (2\hat{\Omega}_c \hat{P}_\varphi)^{1/2} \cos \varphi + \hat{p}_{z'}^2 + 1 \}^{1/2}, \quad (23)$$

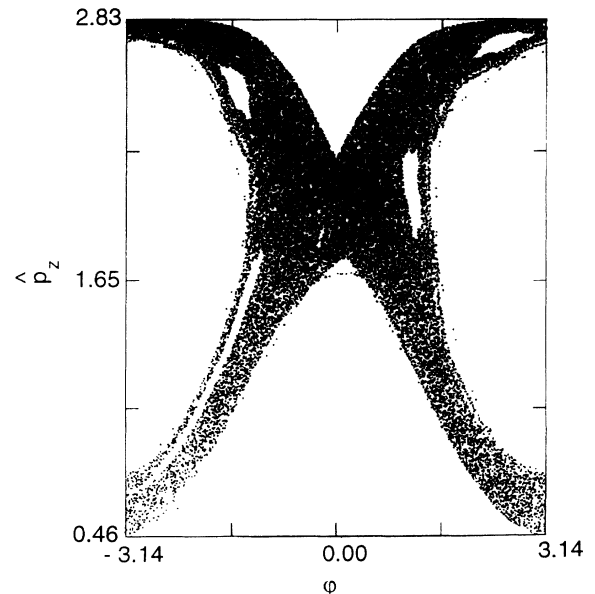


FIG. 7. Surface of section plots corresponding to the trajectory shown in Fig. 1, with  $\Psi = 0 \pmod{2\pi}$ .

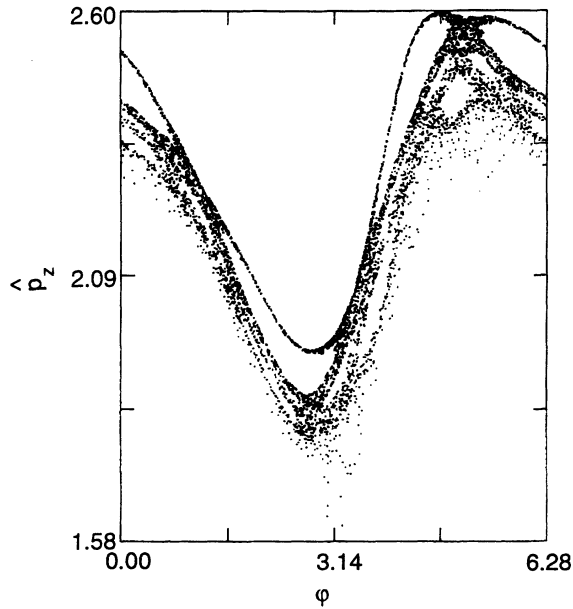


FIG. 8. Surface of section plots corresponding to the trajectory shown when  $\Omega_c$  is larger than its critical value [Lyapunov exponent of Fig. 6(b)], with  $\Psi=0 \pmod{2\pi}$ .

with

$$\hat{\phi}_s = 2\epsilon\hat{\Omega}_c [\hat{P}_\varphi + \hat{P}_\Psi - 2(\hat{P}_\varphi\hat{P}_\Psi)^{1/2} \sin(\varphi + \Psi)] \quad (24)$$

and

$$\hat{p}_z = \hat{P}_z - \hat{P}_\varphi + \hat{P}_\Psi + \beta_b \hat{\phi}_s, \quad (25)$$

which is the normalized axial mechanical momentum. As expected,  $\hat{H}$  is independent of  $\hat{z}'$ .

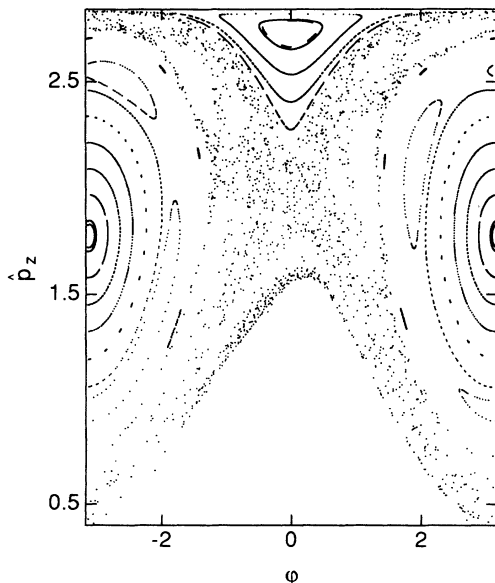


FIG. 9. Surface of section plots for  $n_b = 2 \times 10^{11} \text{ cm}^{-3}$ ,  $\beta_b = 0.91$ ,  $B_0 = 0.715 \text{ T}$ ,  $B_w = 715 \text{ G}$ ,  $\hat{\Omega}_c = 2$ ,  $\hat{H} = 3$ , and for different initial conditions.

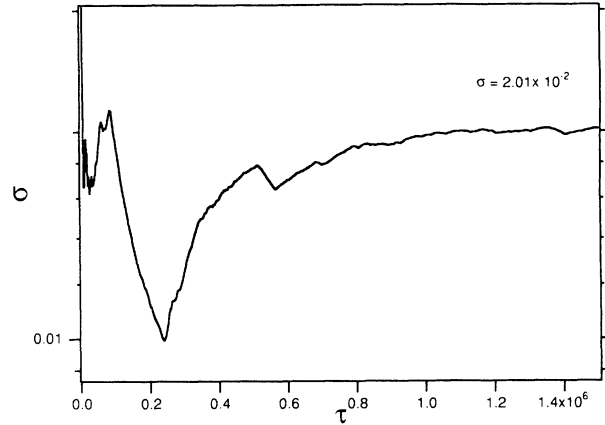


FIG. 10. Lyapunov exponent calculated with the variables of Chen and Davidson [2] and with the same initial conditions as those of Fig. 4.

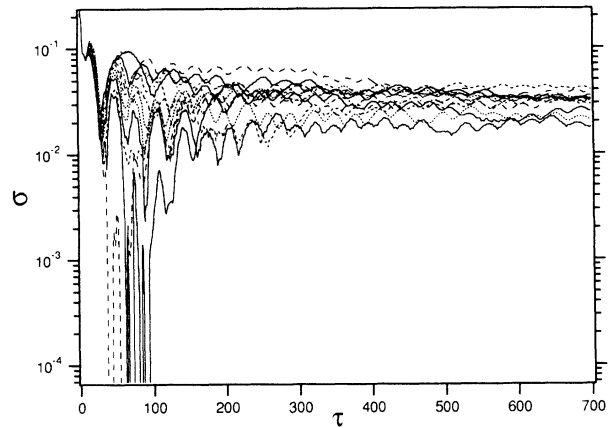


FIG. 11. Local Lyapunov exponents for 12 initial conditions about those of the trajectories considered in Fig. 3. The average value is  $\sigma = 3.01 \times 10^{-2}$ .

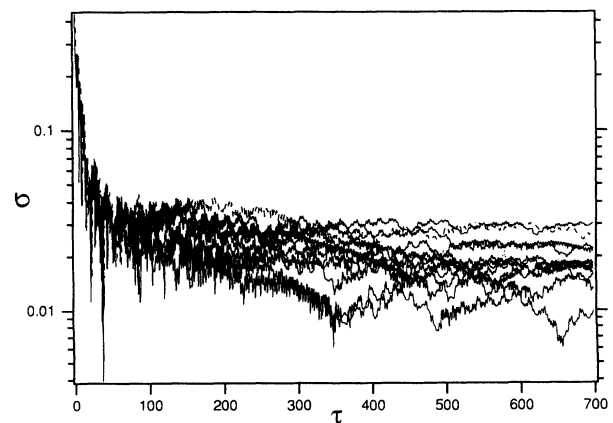


FIG. 12. Local Lyapunov exponents for 12 initial conditions about those of one trajectory used for Fig. 6. The average value is  $\sigma = 1.88 \times 10^{-2}$ .

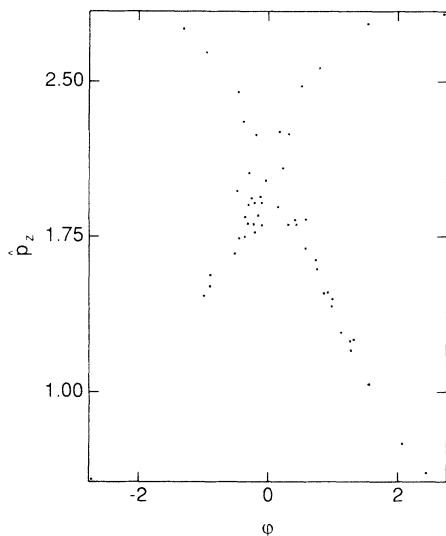


FIG. 13. Same surface of section plot as Fig. 7, with a limited time  $\tau=700$ .

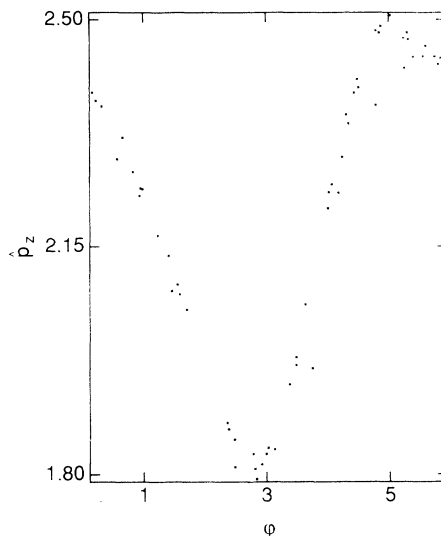


FIG. 14. Same surface of section plot as Fig. 8, with a limited time  $\tau=700$ .

The new variables defined by Eqs. (17)–(22) permit us to describe the motion by four equations instead of six. This improves the accuracy of numerical calculations. To obtain very accurate Poincaré sections, a fourth-order Runge-Kutta method with adaptive step size was used to integrate the equations of motion. The following energy-conservation condition has been verified for each trajectory  $10^{-9} < \Delta H/H < 10^{-6}$ . The Poincaré maps (Figs. 7 and 8) corresponding to the two trajectories were performed using Hénon's method [9] to obtain very accurate intersections with the plane of section  $\Psi=0 \pmod{2\pi}$ . In our case, the step size for the numerical calculation is so small that this method does not modify our results significantly. Figure 9, compared to Fig. 5(a) of Ref. [2(a)], shows that our results are in good agreement with those of Chen and Davidson [2].

The Lyapunov exponent shown in Fig. 4 was calculated again by using the variables of Chen and Davidson. A similar asymptotic result was obtained (see Fig. 10). The existence of a positive Lyapunov exponent is a signature of the chaos in the asymptotic limit. Since the electrons leave the wiggler after a finite time, it is interesting to calculate a "local Lyapunov exponent" [3] for times shorter than or equal to the time they spend in the wiggler. In the vicinity of the initial conditions of the two studied chaotic trajectories, twelve additional initial conditions were chosen (Figs. 11 and 12). An average local Lyapunov exponent was calculated by using these nearby trajectories. It has the same order of magnitude as the asymptotic one. It has been verified that all the local Lyapunov exponents go to zero when the self-fields are neglected. As a consequence, both local and asymptotic exponents give the "mixing time" for trajectories. It is shown on short-time Poincaré sections (Figs. 13 and 14) that the electron visits uniformly the whole ergodic re-

gion of the phase space in the same time as that chosen for the calculation of the local Lyapunov exponents. In the considered stochastic region, electron trajectories will entangle after 8–18 periods of the wiggler. As a consequence, chaos has to be considered in this problem.

### III. DISCUSSION

Efficient numerical tools allowing us to find out whether a trajectory is chaotic or not were suggested. The calculation of Lyapunov exponents was performed and tested by comparing results obtained using different approaches of Benettin's method. The Poincaré maps were calculated with great accuracy. A very stringent condition on energy conservation was used.

A second constant of motion was found by using the symmetry of the problem. It reduces the dimension of phase space and can help to introduce the variables of Chen and Davidson [2]. The chaoticity of some trajectories predicted by calculating nonzero Lyapunov exponents is confirmed by performing Poincaré maps, which are similar to those of Chen and Davidson.

Local Lyapunov exponents were also calculated in order to find the mixing time of the electron trajectories. It was shown that chaos due to the self-fields of the beam can be a crucial problem in an experiment. In the cases considered, the growth length for the chaotic trajectories is 8–18 wiggler periods.

### ACKNOWLEDGMENTS

We would like to thank Professor J. M. Buzzi, Dr. D. Iracane, and Professor L. Friedland for helpful and stimulating discussions. The Laboratoire de Physique des Milieux Ionisés is Unité propre de recherche No. 287 du Centre National de la Recherche Scientifique.

- [1] S. N. Rasband, *Chaotic Dynamics of Nonlinear Systems* (Wiley, New York, 1990); G. Benettin, L. Galgani, and J. M. Strelcyn, *Phys. Rev. A* **14**, 2338 (1976).
- [2] (a) C. Chen and R. C. Davidson, *Phys. Fluids B* **2**, 171 (1990); (b) *Phys. Rev. A* **43**, 5541 (1991).
- [3] F. Varosi, T. M. Antonsen, Jr., and E. Ott, *Phys. Fluids A* **3**, 1017 (1991).
- [4] R. C. Davidson, *Theory of Nonneutral Plasmas* (Benjamin, Reading, MA, 1974).
- [5] G. Spindler and G. Renz, *Phys. Fluids B* **3**, 3517 (1991).
- [6] L. Vallier, *thèse de troisième cycle*, Université d'Orsay, 1983.
- [7] R. G. Littlejohn, A. N. Kaufman, and G. L. Johnson, *Phys. Lett. A* **120**, 291 (1987).
- [8] R. D. Jones, *Phys. Fluids B* **24**, 564 (1981).
- [9] M. Hénon, *Physica D* **5**, 412 (1982).

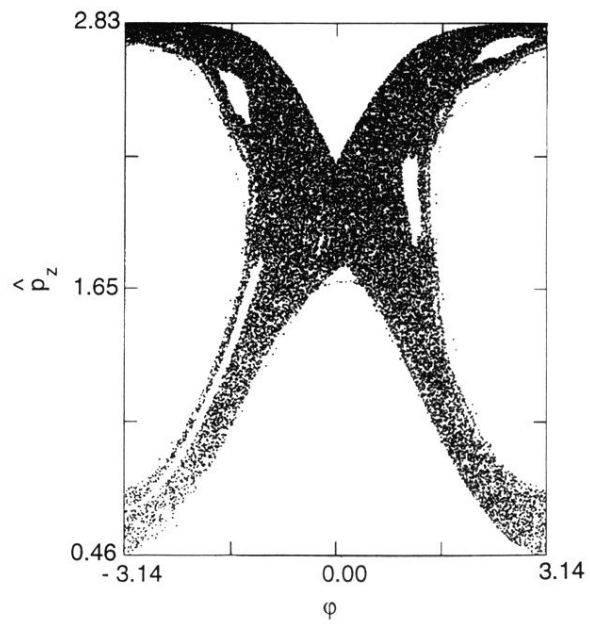


FIG. 7. Surface of section plots corresponding to the trajectory shown in Fig. 1, with  $\Psi=0 \pmod{2\pi}$ .

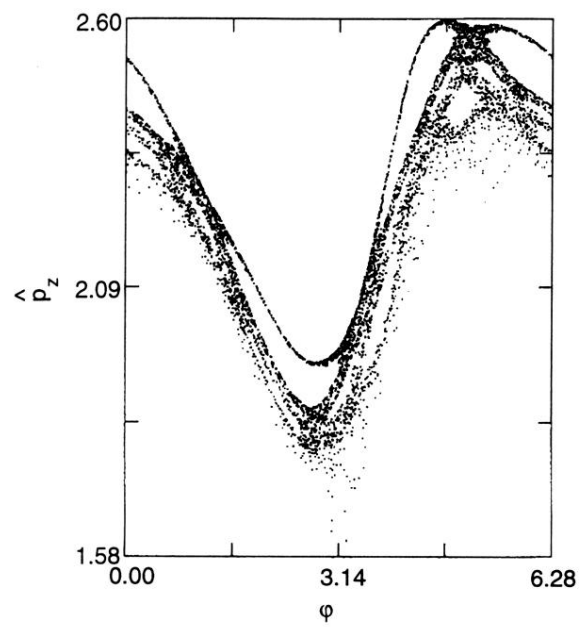


FIG. 8. Surface of section plots corresponding to the trajectory shown when  $\Omega_c$  is larger than its critical value [Lyapunov exponent of Fig. 6(b)], with  $\Psi = 0 \pmod{2\pi}$ .